DESY 95-162

Measurement of the Total Photon Proton Cross Section and its Decomposition at 200 GeV Centre of Mass Energy

H1 Collaboration

Abstract:

We present a new measurement of the total photoproduction cross section performed with the H1 detector at HERA. For an average centre of mass energy of 200 GeV a value of $\sigma_{tot}^{\gamma p} = 165 \pm 2 \pm 11 \mu$b has been obtained. A detailed analysis of the data in adequate kinematic regions enabled a decomposition of the total cross section in its elastic, single diffractive dissociation and remaining non-diffractive parts, based on safe assumptions on the double diffractive dissociation contribution.

H1 Collaboration

S. Aid[14], V. Andreev[26], B. Andrieu[29], R.-D. Appuhn[12], M. Arpagaus[37], A. Babaev[25], J. Bähr[36], J. Bán[18], Y. Ban[28], P. Baranov[26], E. Barrelet[30], R. Barschke[12], W. Bartel[12], M. Barth[5], U. Bassler[30], H.P. Beck[38], H.-J. Behrend[12], A. Belousov[26], Ch. Berger[1], G. Bernardi[30], R. Bernet[37], G. Bertrand-Coremans[5], M. Besançon[10], R. Beyer[12], P. Biddulph[23], P. Bispham[23], J.C. Bizot[28], V. Blobel[14], K. Borras[9], F. Botterweck[5], V. Boudry[29], S. Bourov[25], A. Braemer[15], F. Brasse[12], W. Braunschweig[1], V. Brisson[28], D. Bruncko[18], C. Brune[16], R. Buchholz[12], L. Büngener[14], J. Bürger[12], F.W. Büsser[14], A. Buniatian[12,39], S. Burke[19], M.J. Burton[23], G. Buschhorn[27], A.J. Campbell[12], T. Carli[27], F. Charles[12], M. Charlet[12], D. Clarke[6], A.B. Clegg[19], B. Clerbaux[5], J.G. Contreras[9], C. Cormack[20], J.A. Coughlan[6], A. Courau[28], Ch. Coutures[10], G. Cozzika[10], L. Criegee[12], D.G. Cussans[6], J. Cvach[31], S. Dagoret[30], J.B. Dainton[20], W.D. Dau[17], K. Daum[35], M. David[10], C.L. Davis[19], B. Delcourt[28], L. Del Buono[30], A. De Roeck[12], E.A. De Wolf[5], P. Dixon[19], P. Di Nezza[33], C. Dollfus[38], J.D. Dowell[4], H.B. Dreis[2], A. Droutskoi[25], J. Duboc[30], D. Düllmann[14], O. Dünger[14], H. Duhm[13], J. Ebert[35], T.R. Ebert[20], G. Eckerlin[12], V. Efremenko[25], S. Egli[38], H. Ehrlichmann[36], S. Eichenberger[38], R. Eichler[37], F. Eisele[15], E. Eisenhandler[21], R.J. Ellison[23], E. Elsen[12], M. Erdmann[15], W. Erdmann[37], E. Evrard[5], L. Favart[5], A. Fedotov[25], D. Feeken[14], R. Felst[12], J. Feltesse[10], J. Ferencei[16], F. Ferrarotto[33], K. Flamm[12], M. Fleischer[9], M. Flieser[27], G. Flügge[2], A. Fomenko[26], B. Fominykh[25], M. Forbush[8], J. Formánek[32], J.M. Foster[23], G. Franke[12], E. Fretwurst[13], E. Gabathuler[20], K. Gabathuler[34], J. Garvey[4], J. Gayler[12], M. Gebauer[9], A. Gellrich[12], H. Genzel[1], R. Gerhards[12], A. Glazov[36], U. Goerlach[12], L. Goerlich[7], N. Gogitidze[26], M. Goldberg[30], D. Goldner[9], B. Gonzalez-Pineiro[30], I. Gorelov[25], P. Goritchev[25], C. Grab[37], H. Grässler[2], R. Grässler[2], T. Greenshaw[20], R.K. Griffiths[21], G. Grindhammer[27], A. Gruber[27], C. Gruber[17], J. Haack[36], D. Haidt[12], L. Hajduk[7], O. Hamon[30], M. Hampel[1], M. Hapke[12], W.J. Haynes[6], G. Heinzelmann[14], R.C.W. Henderson[19], H. Henschel[36], I. Herynek[31], M.F. Hess[27], W. Hildesheim[12], P. Hill[6], K.H. Hiller[36], C.D. Hilton[23], J. Hladký[31], K.C. Hoeger[23], M. Höppner[9], R. Horisberger[34], V.L. Hudgson[4], Ph. Huet[5], M. Hütte[9], H. Hufnagel[15], M. Ibbotson[23], H. Itterbeck[1], M.-A. Jabiol[10], A. Jacholkowska[28], C. Jacobsson[22], M. Jaffre[28], J. Janoth[16], T. Jansen[12], L. Jönsson[22], K. Johannsen[14], D.P. Johnson[5], L. Johnson[19], H. Jung[10], P.I.P. Kalmus[21], D. Kant[21], R. Kaschowitz[2], P. Kasselmann[13], U. Kathage[17], J. Katzy[15], H.H. Kaufmann[36], S. Kazarian[12], I.R. Kenyon[4], S. Kermiche[24], C. Keuker[1], C. Kiesling[27], M. Klein[36], C. Kleinwort[14], G. Knies[12], W. Ko[8], T. Köhler[1], J.H. Köhne[27], H. Kolanoski[3], F. Kole[8], S.D. Kolya[23], V. Korbel[12], M. Korn[9], P. Kostka[36], S.K. Kotelnikov[26], T. Krämerkämper[9], M.W. Krasny[7,30], H. Krehbiel[12], D. Krücker[2], U. Krüger[12], U. Krüner-Marquis[12], H. Küster[2], M. Kuhlen[27], T. Kurča[18], J. Kurzhöfer[9], B. Kuznik[35], D. Lacour[30], B. Laforge[10], F. Lamarche[29], R. Lander[8], M.P.J. Landon[21], W. Lange[36], P. Lanius[27], J.-F. Laporte[10], A. Lebedev[26], F. Lehner[12], C. Leverenz[12], S. Levonian[26], Ch. Ley[2], G. Lindström[13], J. Link[8], F. Linsel[12], J. Lipinski[14], B. List[12], G. Lobo[28], P. Loch[28], H. Lohmander[22], J.W. Lomas[23], G.C. Lopez[21], V. Lubimov[25], D. Lüke[9,12], N. Magnussen[35], E. Malinovski[26], S. Mani[8], R. Maraček[18], P. Marage[5], J. Marks[24], R. Marshall[23], J. Martens[35], G. Martin[14], R. Martin[20], H.-U. Martyn[1], J. Martyniak[28], S. Masson[2], T. Mavroidis[21], S.J. Maxfield[20], S.J. McMahon[20], A. Mehta[6], K. Meier[16], D. Mercer[23], T. Merz[12], A. Meyer[12], A. Meyer[14], C.A. Meyer[38], H. Meyer[35], J. Meyer[12], P.-O. Meyer[2], A. Migliori[29], S. Mikocki[7], D. Milstead[20], F. Moreau[29], J.V. Morris[6], E. Mroczko[7], G. Müller[12], K. Müller[12], P. Murín[18], V. Nagovizin[25], R. Nahnhauer[36], B. Naroska[14], Th. Naumann[36], P.R. Newman[4], D. Newton[19], D. Neyret[30], H.K. Nguyen[30], T.C. Nicholls[4], F. Niebergall[14], C. Niebuhr[12], Ch. Niedzballa[1], R. Nisius[1], G. Nowak[7], G.W. Noyes[6], M. Nyberg-Werther[22], M. Oakden[20], H. Oberlack[27], U. Obrock[9], J.E. Olsson[12], D. Ozerov[25], P. Palmen[2], E. Panaro[12], A. Panitch[5], C. Pascaud[28], G.D. Patel[20], H. Pawletta[2], E. Peppel[36], E. Perez[10], J.P. Phillips[20], Ch. Pichler[13], A. Pieuchot[24], D. Pitzl[37], G. Pope[8], S. Prell[12], R. Prosi[12], K. Rabbertz[1], G. Rädel[12],

F. Raupach[1], P. Reimer[31], S. Reinshagen[12], P. Ribarics[27], H. Rick[9], V. Riech[13], J. Riedlberger[37], S. Riess[14], M. Rietz[2], E. Rizvi[21], S.M. Robertson[4], P. Robmann[38], H.E. Roloff[36], R. Roosen[5], K. Rosenbauer[1], A. Rostovtsev[25], F. Rouse[8], C. Royon[10], K. Rüter[27], S. Rusakov[26], K. Rybicki[7], N. Sahlmann[2], D.P.C. Sankey[6], P. Schacht[27], S. Schiek[14], S. Schleif[16], P. Schleper[15], W. von Schlippe[21], D. Schmidt[35], G. Schmidt[14], A. Schöning[12], V. Schröder[12], E. Schuhmann[27], B. Schwab[15], G. Sciacca[36], F. Sefkow[12], M. Seidel[13], R. Sell[12], A. Semenov[25], V. Shekelyan[12], I. Sheviakov[26], L.N. Shtarkov[26], G. Siegmon[17], U. Siewert[17], Y. Sirois[29], I.O. Skillicorn[11], P. Smirnov[26], J.R. Smith[8], V. Solochenko[25], Y. Soloviev[26], J. Spiekermann[9], S. Spielman[29], H. Spitzer[14], R. Starosta[1], M. Steenbock[14], P. Steffen[12], R. Steinberg[2], B. Stella[33], K. Stephens[23], J. Stier[12], J. Stiewe[16], U. Stößlein[36], K. Stolze[36], J. Strachota[31], U. Straumann[38], W. Struczinski[2], J.P. Sutton[4], S. Tapprogge[16], V. Tchernyshov[25], J. Theissen[2], C. Thiebaux[29], G. Thompson[21], P. Truöl[38], J. Turnau[7], J. Tutas[15], P. Uelkes[2], A. Usik[26], S. Valkár[32], A. Valkárová[32], C. Vallée[24], D. Vandenplas[29], P. Van Esch[5], P. Van Mechelen[5], A. Vartapetian[12,39], Y. Vazdik[26], P. Verrecchia[10], G. Villet[10], K. Wacker[9], A. Wagener[2], M. Wagener[34], A. Walther[9], B. Waugh[23], G. Weber[14], M. Weber[12], D. Wegener[9], A. Wegner[27], H.P. Wellisch[27], L.R. West[4], S. Willard[8], M. Winde[36], G.-G. Winter[12], C. Wittek[14], A.E. Wright[23], E. Wünsch[12], N. Wulff[12], T.P. Yiou[30], J. Žáček[32], D. Zarbock[13], Z. Zhang[28], A. Zhokin[25], M. Zimmer[12], W. Zimmermann[12], F. Zomer[28], J. Zsembery[10], K. Zuber[16], and M. zurNedden[38]

[1] *I. Physikalisches Institut der RWTH, Aachen, Germany*[a]
[2] *III. Physikalisches Institut der RWTH, Aachen, Germany*[a]
[3] *Institut für Physik, Humboldt-Universität, Berlin, Germany*[a]
[4] *School of Physics and Space Research, University of Birmingham, Birmingham, UK*[b]
[5] *Inter-University Institute for High Energies ULB-VUB, Brussels; Universitaire Instelling Antwerpen, Wilrijk; Belgium*[c]
[6] *Rutherford Appleton Laboratory, Chilton, Didcot, UK*[b]
[7] *Institute for Nuclear Physics, Cracow, Poland*[d]
[8] *Physics Department and IIRPA, University of California, Davis, California, USA*[e]
[9] *Institut für Physik, Universität Dortmund, Dortmund, Germany*[a]
[10] *CEA, DSM/DAPNIA, CE-Saclay, Gif-sur-Yvette, France*
[11] *Department of Physics and Astronomy, University of Glasgow, Glasgow, UK*[b]
[12] *DESY, Hamburg, Germany*[a]
[13] *I. Institut für Experimentalphysik, Universität Hamburg, Hamburg, Germany*[a]
[14] *II. Institut für Experimentalphysik, Universität Hamburg, Hamburg, Germany*[a]
[15] *Physikalisches Institut, Universität Heidelberg, Heidelberg, Germany*[a]
[16] *Institut für Hochenergiephysik, Universität Heidelberg, Heidelberg, Germany*[a]
[17] *Institut für Reine und Angewandte Kernphysik, Universität Kiel, Kiel, Germany*[a]
[18] *Institute of Experimental Physics, Slovak Academy of Sciences, Košice, Slovak Republic*[f]
[19] *School of Physics and Chemistry, University of Lancaster, Lancaster, UK*[b]
[20] *Department of Physics, University of Liverpool, Liverpool, UK*[b]
[21] *Queen Mary and Westfield College, London, UK*[b]
[22] *Physics Department, University of Lund, Lund, Sweden*[g]
[23] *Physics Department, University of Manchester, Manchester, UK*[b]
[24] *CPPM, Université d'Aix-Marseille II, IN2P3-CNRS, Marseille, France*
[25] *Institute for Theoretical and Experimental Physics, Moscow, Russia*
[26] *Lebedev Physical Institute, Moscow, Russia*[f]
[27] *Max-Planck-Institut für Physik, München, Germany*[a]
[28] *LAL, Université de Paris-Sud, IN2P3-CNRS, Orsay, France*
[29] *LPNHE, Ecole Polytechnique, IN2P3-CNRS, Palaiseau, France*
[30] *LPNHE, Universités Paris VI and VII, IN2P3-CNRS, Paris, France*
[31] *Institute of Physics, Czech Academy of Sciences, Praha, Czech Republic*[f,h]

[32] Nuclear Center, Charles University, Praha, Czech Republic[f,h]
[33] INFN Roma and Dipartimento di Fisica, Universita "La Sapienza", Roma, Italy
[34] Paul Scherrer Institut, Villigen, Switzerland
[35] Fachbereich Physik, Bergische Universität Gesamthochschule Wuppertal, Wuppertal, Germany[a]
[36] DESY, Institut für Hochenergiephysik, Zeuthen, Germany[a]
[37] Institut für Teilchenphysik, ETH, Zürich, Switzerland[i]
[38] Physik-Institut der Universität Zürich, Zürich, Switzerland[i]
[39] Visitor from Yerevan Phys.Inst., Armenia

[a] Supported by the Bundesministerium für Forschung und Technologie, FRG under contract numbers 6AC17P, 6AC47P, 6DO57I, 6HH17P, 6HH27I, 6HD17I, 6HD27I, 6KI17P, 6MP17I, and 6WT87P
[b] Supported by the UK Particle Physics and Astronomy Research Council, and formerly by the UK Science and Engineering Research Council
[c] Supported by FNRS-NFWO, IISN-IIKW
[d] Supported by the Polish State Committee for Scientific Research, grant Nos. SPUB/P3/202/94 and 2 PO3B 237 08, and Stiftung fuer Deutsch-Polnische Zusammenarbeit, project no.506/92
[e] Supported in part by USDOE grant DE F603 91ER40674
[f] Supported by the Deutsche Forschungsgemeinschaft
[g] Supported by the Swedish Natural Science Research Council
[h] Supported by GA ČR, grant no. 202/93/2423, GA AV ČR, grant no. 19095 and GA UK, grant no. 342
[i] Supported by the Swiss National Science Foundation

1 Introduction

The total cross section is an important quantity related to the fundamental properties of particle interactions. Although measurements are available for hadron hadron and real photon hadron collisions at low energy [1], so far only the data from $p\bar{p}$-colliders provide precise information on the rise of the total cross section at high energy. The ep collider HERA, with e and p energies of 27.6 and 820 GeV, provides a new source of information on high energy photon proton collisions.

The interaction of electrons and protons at the HERA collider is dominated by photoproduction processes, in which the electron scatters through small angles emitting a quasi-real photon, which then interacts with the proton. Recently the total photoproduction cross section has been measured at HERA at a γp CMS energy of 195 GeV by H1 [2] $\sigma_{tot}^{\gamma p} = 156 \pm 18$ μb [1] and at a γp CMS energy of 180 GeV by ZEUS [3] $\sigma_{tot}^{\gamma p} = 143 \pm 17$ μb. These measurements confirmed the expected rise of the total γp cross section with energy. However, large systematic uncertainties do not yet allow discrimination between different models predicting a moderate rise of the γp total cross section [4-8]. In the previous H1 analysis [2], the systematic error is dominated by the assumptions on the partial γp cross sections, which is important as they have different acceptance. ZEUS [3] determined the fraction of γp diffractive events directly from the data and thus reduced the model dependence of the result. However, the precision of this measurement is limited by the large systematic error in the efficiency of tagging the scattered electrons.

In this paper a new determination of $\sigma_{tot}^{\gamma p}$ at the average centre of mass energy $W_{\gamma p} = 200$ GeV is presented. Dedicated trigger conditions, specially designed for high energy photoproduction, allow the measurement of the diffractive components of the γp cross sections and, therefore, substantially reduce the model dependence in the acceptance calculations. This, together with a better understanding of the electron tagging efficiency improves the accuracy of the $\sigma_{tot}^{\gamma p}$ measurement compared with the earlier results from HERA.

The data used in the present analysis were taken during a period in which HERA was operated with a positron beam. Nevertheless, "electron" is used as generic term for the HERA beam lepton throughout this paper.

2 Photoproduction

In ep collisions the total photoproduction cross section, $\sigma_{tot}^{\gamma p}$ can be related to the total differential ep cross section by the Weizsäcker-Williams formula [9] for the photon flux $F(y, Q^2)$

$$\frac{d^2\sigma^{ep}(s)}{dydQ^2} = \sigma_{tot}^{\gamma p}(ys) \cdot (1 + \delta_{RC}) \cdot F(y, Q^2) =$$

$$= \sigma_{tot}^{\gamma p}(ys) \cdot (1 + \delta_{RC}) \cdot \frac{\alpha}{2\pi Q^2}\Big(\frac{1 + (1-y)^2}{y} - \frac{2(1-y)}{y} \cdot \frac{Q^2_{min}}{Q^2}\Big), \qquad (1)$$

where Q^2 is the negative square of the photon 4-momentum, or the virtuality of the photon, and s is the squared centre of mass energy of the ep interaction. For small scattering angles, y is defined as $1 - E'_e/E_e$, where E_e and E'_e are the energies of the initial and scattered electron respectively. The minimum photon virtuality is $Q^2_{min} = (m_e y)^2/(1-y)$. The factor $(1 + \delta_{RC})$ takes into account QED radiative corrections to the ep Born cross section. In the formula (1) a dependence of $\sigma_{tot}^{\gamma p}$ on Q^2 and a contribution of longitudinally polarized photons are neglected. These are good approximations in the present kinematic conditions [10].

[1]Note that this number underestimates $\sigma_{tot}^{\gamma p}$ by 6–7% due to the approximation used in the theoretical expression for the photon flux.

Hadronic final states produced in real photon proton collisions resemble those observed in hadron hadron collisions. This similarity led to the phenomenological approach to describe photoproduction by the so called Vector Meson Dominance (VMD) model [11], where the photon first converts into a vector meson (predominantly the ρ^0) which then interacts with the proton. As in hadron hadron collisions, the total γp cross section has a substantial contribution from diffractive γp reactions, which have a final state topology radically different from the bulk of non-diffractive events. Since diffractive reactions involve no exchange of quantum numbers between the incident particles, the final state is characterized by the appearance of large rapidity intervals, or gaps, with no hadrons. This feature of diffractive events is exploited below to determine their contributions to the γp cross section. We distinguish the following diffractive processes in photoproduction:

- Elastic vector meson production (EL) $\gamma + p \rightarrow V + p$, where V stands for one of the vector mesons ρ^0, ω, ϕ. The true electro-magnetic elastic reaction $\gamma + p \rightarrow \gamma + p$ has a very low cross section and is neglected [11].
- Single photon diffractive dissociation (GD) $\gamma + p \rightarrow X + p$, where the photon dissociates into the heavy hadronic state X and the proton stays intact.
- Single proton diffractive dissociation (PD) $\gamma + p \rightarrow V + Y$, where the proton dissociates into a hadronic state Y and a vector meson is produced in the photon direction.
- Double diffractive dissociation (DD) $\gamma + p \rightarrow X + Y$, where both the photon and the proton dissociate.

For the last three diffractive reactions the cross section is considered for the full momentum transfer range and for masses (M) of the dissociating system obeying $M^2 < 0.1 W_{\gamma p}^2$, where $W_{\gamma p}$ is the centre of mass energy. The value 0.1 is chosen to enable direct comparisons with measurements of the diffractive cross section from hadron colliders and fixed target photoproduction experiments as well as with available theoretical calculations.

All processes $\gamma + p \rightarrow X$ not belonging to the contributions defined above are called non-diffractive (ND). These processes dominantly involve exchange of quantum numbers between the photon and the proton.

3 Monte Carlo Models for Photoproduction

Two Monte Carlo (MC) models, based on the event generators PYTHIA [12] and PHOJET [13], are used for the acceptance calculation. Both models include all the diffractive and non-diffractive contributions to the γp cross section discussed above.

The model for non-diffractive events in the PYTHIA program is similar to the multiple-interaction model developed for hadron hadron collisions [14]. An eikonal approach is used, in which the rate of jets above a transverse momentum $p_{\perp\min}$ (the default value $p_{\perp\min} = 1.45$ GeV/c is taken) is combined with a parameterization of the non-diffractive total cross section to calculate a probability distribution in the number of semi-hard interactions. For events below this cut-off two longitudinal strings are stretched between the proton and the “VMD-photon”, to give a representation of an event structure caused by soft gluon exchange.

Events with elastic, diffractive single and double dissociation scattering in the PYTHIA MC model have the same general structure: the t-dependence is given by a function $\exp(Bt)$, where t is the square of the four-momentum transfer in the diffractive reaction and B is the nuclear slope parameter. Within the energy range used in this analysis the nuclear slope for elastic vector meson production is $B \approx 11$ (GeV/c)$^{-2}$. A ρ^0 formed by $\gamma \to \rho^0$ in elastic or diffractive scattering is transversely polarized and therefore its decay angular distribution in $\rho^0 \to \pi^+\pi^-$ is taken to be proportional to $\sin^2\theta$, where the reference axis is given by the ρ^0 direction of motion. The relative rates of ρ^0, ω, ϕ production are assumed to be about $13 : 1.5 : 1$ [11].

In single diffractive dissociation, the B-slope is assumed to be half that of elastic scattering. The events are generated according to a dM^2/M^2 distribution for the dissociation system of mass M. The mass spectrum of the system is assumed to start at 0.2 GeV/c^2 above the mass M_{in} of the incoming particle (using the ρ^0 mass for the incoming γ). A light dissociated system, with a mass less than 1 GeV above the mass of the incoming particle, is taken to decay isotropically into a two-body state. Single-resonance states, such as N^* or $\omega(1600)$, are not generated explicitly, but are described in this average manner. A more massive system is treated as a string stretched along the γp interaction axis. The secondary hadrons from the string decay are distributed in a longitudinal phase space with limited transverse momentum.

In the event generator PHOJET, the multi-particle non-diffractive final states are constructed from a parameterization of the photon proton scattering amplitude in an eikonal approximation using the two-component Dual Parton Model [15]. The coding of the model is similar to that of the MC generator DTUJET [16] simulating particle production in pp and $\bar{p}p$ collisions up to very high energies.

In the generator PHOJET elastic vector meson production is similar to that in the PYTHIA model. For diffractive dissociation the PHOJET model assumes a mass dependent nuclear slope B [17]. This slope parameterization gives a steady transition from elastic scattering to single and double diffractive dissociation. The mass spectrum is generated according to a $dM^2/(M^2 - M_{in}^2)$ distribution starting from two pion masses above the mass M_{in} (using the ρ^0 mass for the incoming γ). The low-mass resonance structure is taken into account in an approximate way to provide a phenomenological description of the dissociated mass spectrum observed experimentally [18, 19]. To take the transverse polarization of the incoming photon into account, the decay of the elastically produced vector meson resonances into two or three particles is performed in the s-channel helicity frame according to the angular distributions given in [11]. In addition to resonances, a continuous multi-particle final state in diffraction is generated by simulating a pomeron-proton or pomeron-photon scattering exactly as in the Dual Parton Model used for photon hadron scattering. The pomeron is treated like a virtual meson. The soft and hard scatterings in diffraction are generated according to cross sections given by Regge-parameterizations and the QCD Parton Model, respectively.

The generated events are fed into the H1 detector simulation program and are subject to the same reconstruction and analysis chain as the real data.

The QED radiative corrections are calculated using the HERACLES MC program [20]. This takes into account single photon emission from the lepton line as well as the self energy correction to the Born photoproduction cross section.

4 H1 Detector

A detailed description of the H1 apparatus can be found elsewhere [21]. A schematic layout of the central H1 detector components is shown in Fig. 1. In the following we briefly describe the components of the detector relevant for this analysis.

Measurements of charged particle tracks and the interaction vertex are provided by central and forward tracking systems, both consisting of drift and multi-wire proportional chambers (MWPC). The central and forward track chambers cover the complete azimuthal range and

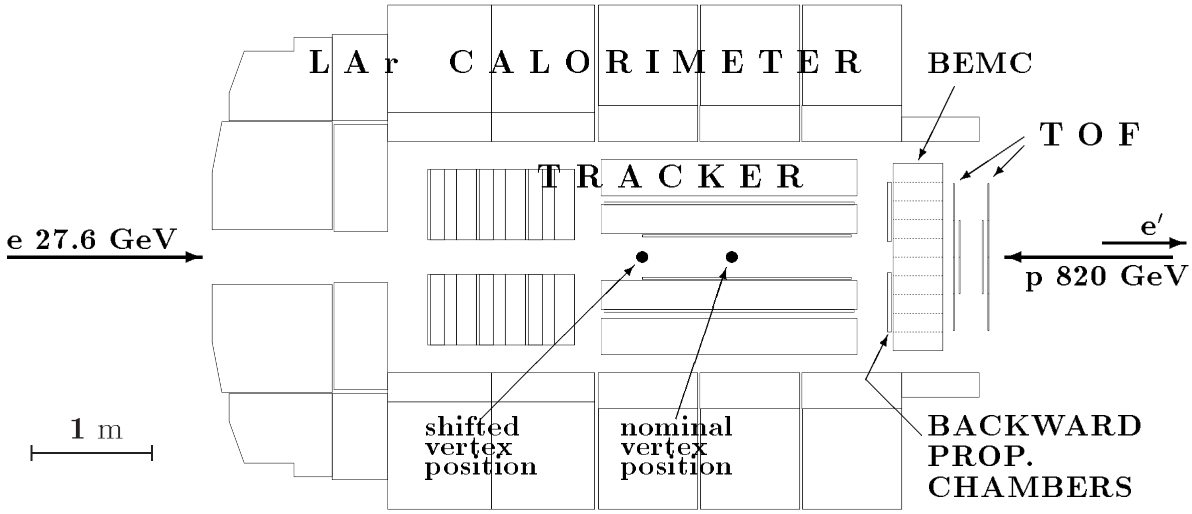

Figure 1: A layout of the central part of the H1 detector.

$-2.0 < \eta < 3.0$ in pseudo-rapidity $\eta = -\ln(\tan\frac{\theta}{2})$. Here θ is the polar angle with respect to the proton beam direction (positive z axis). The central jet chamber (CJC) is interleaved with inner and outer double layers of MWPC, which were used in the trigger to select events with charged tracks pointing to the interaction region. This MWPC system covers the range $-1.5 < \eta < 1.5$. A backward proportional chamber (BPC), with an acceptance of $-3.0 < \eta < -1.5$ allows efficient detection of charged particles produced at large θ.

The tracking region is surrounded by a fine grained liquid argon (LAr) calorimeter [22] consisting of an electro-magnetic and a hadronic section. The total depth of the LAr calorimeter varies between 4.5 and 8 hadronic interaction lengths. Under test beam conditions it has an energy resolution $\sigma/E \approx 12\%/\sqrt{E/\mathrm{GeV}} \oplus 0.01$ for electrons and $\approx 50\%/\sqrt{E/\mathrm{GeV}} \oplus 0.02$ for pions. The LAr calorimeter covers the complete azimuthal range and $-1.5 < \eta < 3.3$. The calorimeter is surrounded by a super-conducting solenoid providing a uniform magnetic field of 1.15 T parallel to the beam axis in the tracking region.

The time of flight system (ToF) is located at $z \approx -2\,\mathrm{m}$ behind the Backward Electro-Magnetic Calorimeter (BEMC), which is about one hadronic interaction length deep. ToF is a hodoscope consisting of two planes of plastic scintillators mounted perpendicular to the beam direction. The angular coverage of the ToF counters corresponds to $-3.5 < \eta < -2$. Having a time resolution better than 2 ns the ToF system enables efficient separation of ep interaction events from the upstream background. In the present analysis the ToF system is included in the trigger for photoproduction events. The efficiency of the ToF counters has been measured using muons in the proton beam halo and corresponds to $(98 \pm 1)\%$ for minimum ionizing particles.

The luminosity system measuring the reaction $ep \to e\gamma p$ consists of two TlCl/TlBr crystal calorimeters. The small angle electron detector (electron tagger) is located at $z = -33\,\mathrm{m}$ and is also used to trigger on photoproduction events. Its 7×7 crystal matrix (an individual crystal measures 2.2×2.2cm) accepts electrons with an energy between $0.2E_e$ and $0.8E_e$ and scattering angles $\theta' \leq 5\,\mathrm{mrad}$ ($\theta' = \pi - \theta$), corresponding to $Q^2 < Q^2_{max} = 0.01$ GeV^2. The photon detector is located at $z = -103\,\mathrm{m}$ and consists of a 5×5 crystal matrix. Both calorimeters are 22 radiation length deep and their energy resolution in the present data taking period was measured to be $\sigma(E)/E = 0.15/\sqrt{E/\mathrm{GeV}} \oplus 0.01$.

5 Luminosity Measurement and Tagging Efficiency

The basic requirement used to tag quasi-real photoproduction processes in H1 is the detection of the scattered electron in the electron tagger. This guarantees very low $Q^2 < 10^{-2}$ GeV^2. Three main ingredients contribute to the overall precision of the measurement of the cross section $\sigma_{tot}^{\gamma p}$: the luminosity measurement error, the knowledge of the electron tagger acceptance and the efficiency of the main apparatus for triggering and reconstruction of the hadronic final states produced in photon proton collisions. The first two are discussed in this section.

The luminosity measurement utilizes the Bethe-Heitler (BH) process $ep \to e\gamma p$ [23]. Several methods for the measurement of the BH process can be exploited and they are described in detail in [24]. In this analysis the method based on the measurement of the photon energy spectrum with $E_\gamma > E_{min} \simeq 8$ GeV is used. The value of E_{min} is chosen such that it is well above the photon detector trigger threshold. The error in the luminosity measurement is then dominated by the precision of the energy calibration and by the correction for the complex structure of

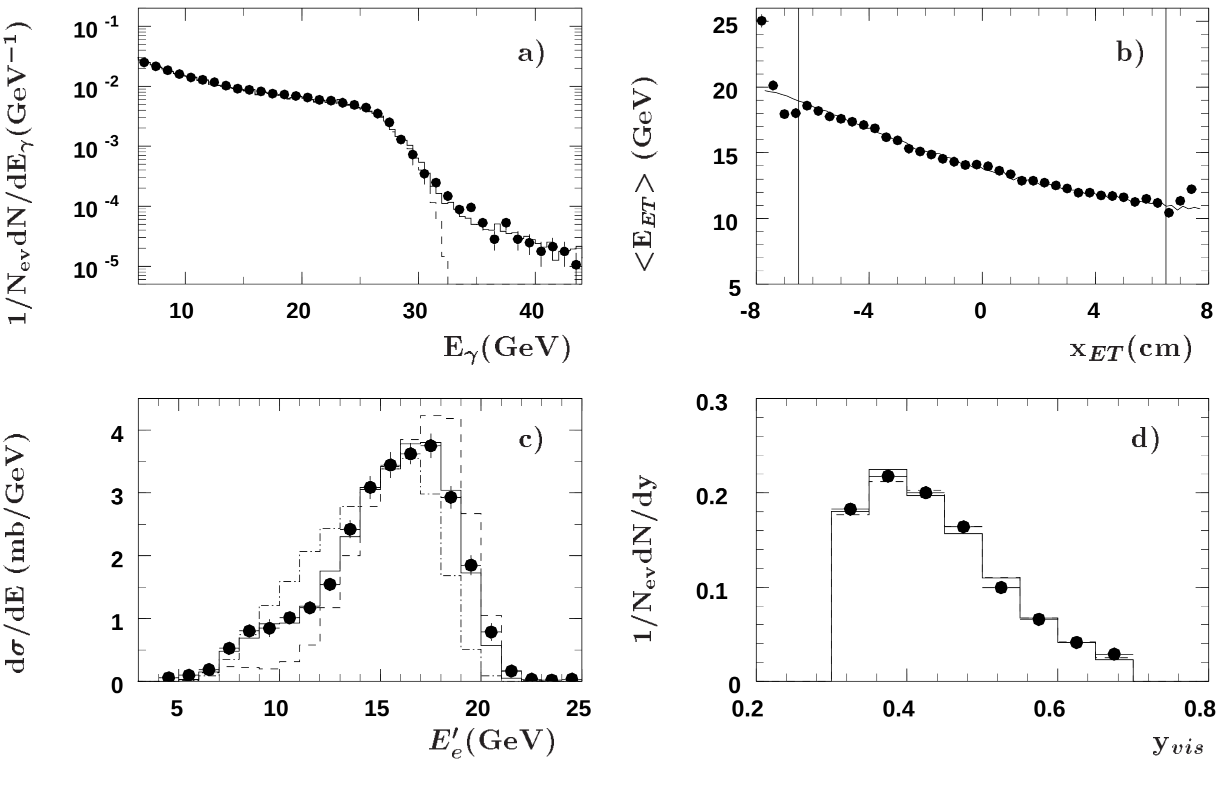

Figure 2: Performance of the H1 luminosity system and the electron tagger acceptance. (a) Normalized photon energy distribution for Bethe-Heitler events in the data (symbols) and Monte Carlo with (full line) and without (dashed line) the event pile-up effect. (b) Correlation between the energy and the lateral coordinate of the impact point of scattered electrons in the electron tagger in the data (symbols) and Monte Carlo (full line). Vertical lines indicate the fiducial cut $|x_{ET}| < 6.5$ cm used in the analysis. (c) Energy spectrum in the electron tagger for Bethe-Heitler events; data (symbols) are compared to MC with measured e-beam tilt $\theta_x = -0.13$ mrad and different offset values of the electron trajectory in the H1 interaction point: $x_{\text{off}} = -0.5$mm, +0.5mm, +1.5mm (dashed, full and dashed-dotted lines respectively). (d) y-distribution in the electron tagger for γp events in the range $0.3 < y < 0.7$ used in this analysis. The points represent the H1 data, histograms are Monte Carlo predictions for the models PYTHIA (solid) and PHOJET (dashed).

the proton bunches – the so called "satellite bunch" effect [24]. After the final absolute energy calibration of the luminosity detectors the observed photon energy spectrum is shown in Fig. 2a. It is well described by the BH process simulation taking into account energy resolution and pile-up effects (ie. several overlapping $ep \to e\gamma p$ events in the same bunch crossing). The precision of the integrated luminosity measurement in different 1994 data samples varies between 1.5% and 5.6%.

The electron tagger performs a double function. It both tags γp events and provides a measurement of the scaling variable y. Since the precision of the energy and coordinate reconstruction is not good enough in the areas close to the detector boundaries, $x_{ET} = \pm 7.7$ cm, a fiducial cut $|x_{ET}| < 6.5$ cm is used in the analysis (Fig. 2b). A corresponding cut on $|y_{ET}|$ is redundant because of the confinement to the HERA bending plane.

The acceptance $A(y, Q^2)$ of the electron tagger for scattered electrons depends strongly on the HERA electron beam optics, being most sensitive to the horizontal tilt θ_x and the horizontal offset $\Delta x_{\rm off}$ with respect to the reference trajectory at the H1 interaction point. The electron beam tilt (typically 0.1 mrad) can be measured with a precision of ± 0.02 mrad by monitoring the position of the photon spot at the photon detector. The offset is not measured directly. The acceptance $A^{BH}(y)$, integrated over Q^2, can be determined using $ep \to e\gamma p$ events. However, $A^{BH}(y)$ differs from the acceptance for photoproduction $A(y)$ due to the different Q^2 dependences.

The following procedure has been used to determine $A(y)$ for any data sample with constant beam conditions. First, the acceptance $A^{BH}(y)$ was measured from $ep \to e\gamma p$ events. Then the Monte Carlo program simulating the H1 luminosity system together with the HERA beam optics was tuned to the data by varying $\Delta x_{\rm off}$, which is the only free parameter in the procedure. Fig. 2c illustrates the sensitivity of the energy distribution in the electron tagger (and thus $A^{BH}(y)$) to the horizontal offset of the reference trajectory. A precision of $\Delta x_{\rm off} = \pm 0.2$ mm has been achieved by this procedure. Finally, the acceptance $A(y)$ was calculated using the measured tilt θ_x and the tuned value of $\Delta x_{\rm off}$. The errors have been estimated from calculations of $A^{BH}(y)$ using extreme values of the parameters. A limited range of $0.3 < y < 0.7$ was used in the analysis, to avoid tails where the acceptance value is less than 20%. Within this interval, errors between 3% and 5% were obtained in the value of $\int A(y)dy$ for different data samples. We therefore conclude that 5% can be used as a conservative estimate of the precision to which the electron tagger acceptance is known in this analysis. Fig. 2d shows the comparison of the y distributions in the data with Monte Carlo, using the two different models for photoproduction as described in section 3.

6 Trigger Conditions and Event Selection

The data used for the measurement of $\sigma_{tot}^{\gamma p}$ were collected in a short dedicated period during the 1994 data taking. The HERA machine was operated with 153 colliding bunches of 27.6 GeV positrons and 820 GeV protons. In addition, 32 "pilot" bunches, 17 proton and 15 positron, had no counterpart and produced no ep collisions enabling an estimate of the beam induced background. Two data samples were collected with different mean z-positions of the ep interaction vertex: the nominal position at $\bar{z} = 4$ cm and a position shifted in the proton direction at $\bar{z} = 71$ cm (see Fig. 1).

The data collected with the nominal vertex position correspond to the integrated luminosity of 23.8 ± 0.4 nb^{-1}, while the shifted vertex position data correspond to 23.8 ± 1.3 nb^{-1}. The advantage of the shifted vertex data is the higher acceptance for diffractive reactions in the region where diffractive processes can be separated safely from the majority of non-diffractive events.

The data were taken with two independent trigger conditions. The first trigger condition, termed "ToF-trigger", is formed by the coincidence of a signal from the electron tagger ($E'_e > 4$ GeV) with a signal from the ToF system coming within the time interval expected for ep interactions. The ToF-trigger is fired by hadrons originating from photon fragmentation. This trigger is efficient for all classes of photoproduction events including elastic vector meson production, although it is affected by the BEMC material in front of the ToF system. The ToF trigger was enabled in both data samples.

The second trigger condition, termed "Ray-trigger", requires a coincidence of the electron detector signal with at least one track pointing to the vertex region. The track condition is derived from the cylindrical MWPC and requires a $p_T \gtrsim 200$ MeV/c. This trigger has been used in previous H1 analyses [2]. In the present analysis the Ray-trigger is used for cross checks and was activated during the run with nominal vertex position only.

Both Ray- and ToF-triggers require in addition the energy in the photon detector to be less than 2 GeV. This condition substantially reduces the size of QED radiative corrections and also suppresses accidental coincidences of Bethe-Heitler events with beam induced background.

The triggered events are subjected to several offline cuts. The fractional energy of the photon, as measured by the electron tagger, is required to be in the interval $0.3 < y < 0.7$. The event vertex, reconstructed from tracks in the CJC, must be within ± 30 cm of the mean z-position of the interaction point. The vertex z-position distribution has a Gaussian shape with a sigma of 10 cm reflecting the length of the proton bunches. For ToF-triggered events at least one reconstructed track in the CJC or in the BPC is required in addition. Similarly the Ray-triggered events are required to have at least one CJC track in the region covered by the Ray-trigger.

Several sources of background contribute to the data samples. The main background source in the ToF-triggered event samples is electron interactions with residual gas ("beam-gas") or with material inside the beam-pipe ("beam-wall"). This contribution is estimated using the data from the non-colliding (pilot) electron bunches and amounts to 4% and 8% respectively, in the event samples with shifted and non-shifted vertex. For Ray-triggered events this background is negligible. Another major source of background originates from accidental coincidences of the electron tagger signal with events resulting from proton beam-gas collisions within the nominal ep interaction region. This contribution is estimated using special monitoring triggers, with looser triggering conditions, and is about 3% in the Ray-triggered data sample. For the ToF-triggered events this background is negligible. Still another type of background stems from the accidental coincidence of electron beam induced background with a Bethe-Heitler process induced signal in the electron tagger. This coincidence appears as background when the associated photon escapes detection in the photon detector, due to the small inefficiency of this detector. From the measured rate of the Bethe-Heitler process this background contribution is estimated to be about 1% in all data samples. Finally there is a small background contribution in all data samples from the QED 2-photon lepton pair production processes, with one photon emitted from the incident electron and the other photon emitted from the proton. This background was calculated using the LPAIR MC event generator [25] and amounts to less than 0.2% under the present trigger and selection conditions. The selected event samples vary between about 19,000 and 22,000 events. The background is subtracted on a statistical basis in the analysis.

Fig. 3 shows a comparison between the nominal vertex ToF-triggered data sample and the two MC simulations. In Fig. 3a the z-position of the reconstructed event vertex is shown and in Fig. 3b-d the multiplicity, transverse momentum and pseudo-rapidity of charged tracks are given. Events with no CJC tracks (i.e. events which fulfil the BPC requirement) do not contribute in the distributions of Fig. 3a, c and d. The agreement between data and simulations demonstrates that the MC event generators reproduce well the main features seen in the data. Especially the z-vertex distribution in Fig. 3a shows that the background contamination in the data is small. Similar comparisons (not shown) for the Ray-triggered event sample lead to the same conclusion.

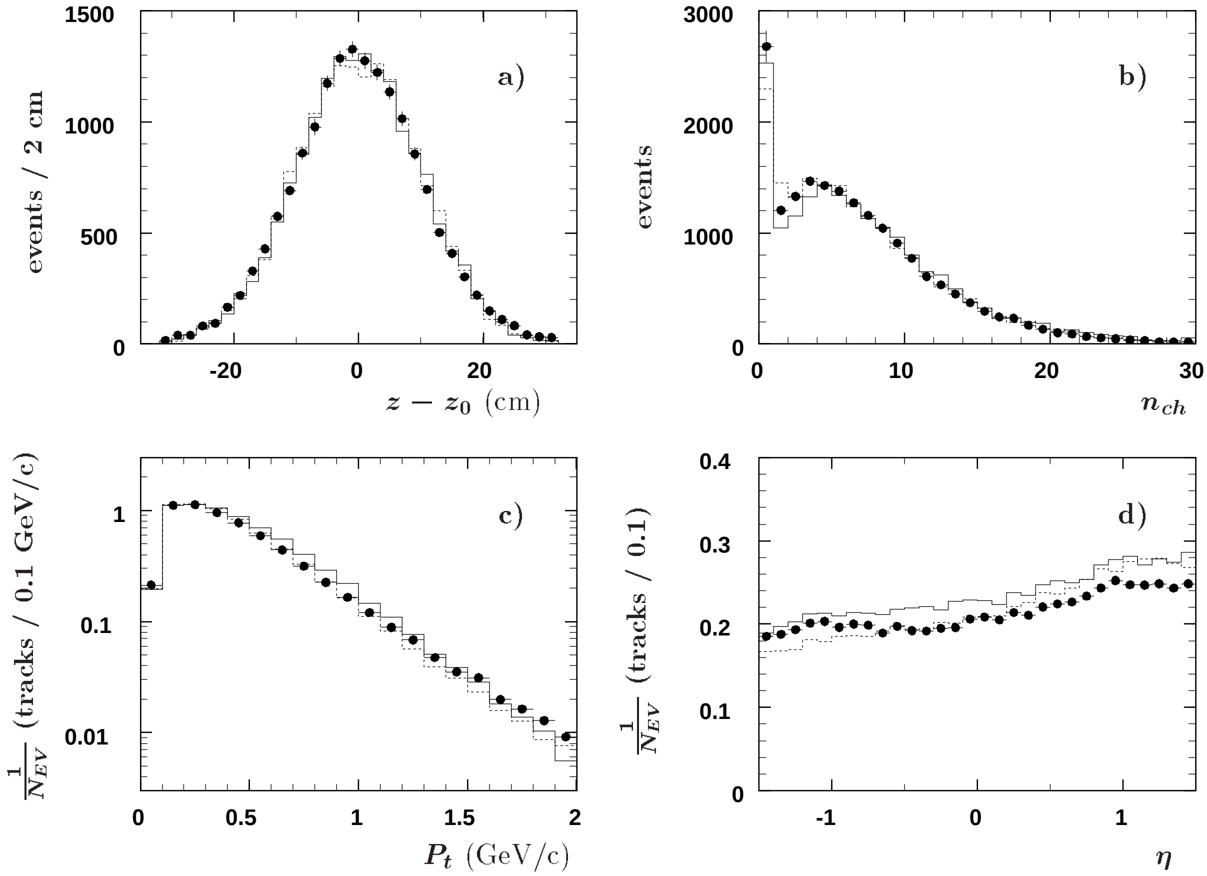

Figure 3: The measured z-position of the reconstructed event vertex (a), multiplicity (b), P_t (c) and η (d) distributions of charged tracks in the data (points) for the nominal vertex sample compared with those in MC simulation using PHOJET (full histogram) and PYTHIA (dotted histogram).

7 Cross Section Calculation Method

For each data sample the observed number of events N is related to the differential ep cross section (1) by the expression

$$\frac{dN}{dydQ^2} = \mathcal{L} \cdot \varepsilon(y) \cdot A(y, Q^2) \cdot \frac{d^2\sigma^{ep}}{dydQ^2}, \tag{2}$$

where $\mathcal{L}$ is the integrated luminosity, $\varepsilon(y)$ is the efficiency of the trigger and selection criteria for the main H1 detector, and $A(y, Q^2)$ is the acceptance of electron tagging as described above. The $A(y, Q^2)$ is factorized out since it depends only on the parameters of the scattered electron and not on the details of the photoproduction process. We assume $\varepsilon(y)$ to be independent of Q^2 since the transverse momentum of the scattered electron is always small. Integrating equation (2) over y and Q^2 in the range from y_{min} to y_{max} and from Q^2_{min} to Q^2_{max} gives

$$N = (1 + \delta_{RC}) \cdot \mathcal{L} \cdot F \cdot A \cdot \varepsilon \cdot \sigma^{\gamma p}_{tot}, \tag{3}$$

using the photon flux integral F and averaged values [2] of A, ε and the cross section $\sigma^{\gamma p}_{tot}$. An identical expression also holds for any partial cross section σ_i with only ε depending on the

[2] A strict definition of the quantities averaged over y and Q^2 is
$\sigma^{\gamma p}_{tot} = \int \sigma^{\gamma p}_{tot}(ys)\varepsilon(y)A(y)F(y)dy / \int \varepsilon(y)A(y)F(y)dy$, $F = \int F(y)dy$, $A = \int A(y)F(y)dy/F$,
$\varepsilon = \int \varepsilon(y)A(y)F(y)dy/AF$, with $F(y) = \int F(y, Q^2)dQ^2$ and $A(y) = \int A(y, Q^2)F(y, Q^2)dQ^2/F(y)$

sub-process i. Therefore, one has for their sum

$$N = (1 + \delta_{RC}) \cdot \mathcal{L} \cdot F \cdot A \cdot \sum \varepsilon_i \sigma_i. \quad (4)$$

Eq.(4) is also valid for the number of events in any kinematic domain of the photoproduction process, with ε_i determined accordingly. This enables us to find the partial cross sections by considering appropriate kinematic regions, enriched by different sub-processes, and solving a (generally over-constrained) system of equations for the σ_i, with efficiencies ε_i calculated by MC simulations.

For our basic kinematic limits of $y_{min} = 0.3$, $y_{max} = 0.7$ (corresponging to the range $165 < W_{\gamma p} < 252$ GeV) and $Q^2_{max} = 0.01$ GeV^2 we find $F = 0.0136$ and the acceptance A varying from 0.546 to 0.570 depending on beam conditions. This variation of A is properly taken into account in the analysis. The MC efficiencies ε_i for the selected ToF-triggered samples are presented in Table 1 . The average value of the radiative correction δ_{RC} is estimated to be $(-1 \pm 1)\%$ and $(+1 \pm 1)\%$ for the ToF- and Ray-trigger samples, respectively.

Table 1: Efficiencies ε_i (%) for the different subprocesses of γp scattering as calculated using the Monte Carlo simulation based on the PHOJET(PYTHIA) models for various data samples. The $\eta_{max} < 0$ and $\eta_{min} > 1$ samples are used to find the diffractive contributions.

sample	*sub-sample*	*subprocess*				
		GD	*PD*	*DD*	*EL*	*ND*
shifted vertex ToF trigger	all events	74(77)	68(71)	71(73)	57(54)	61(65)
	$\eta_{max} < 0$	31(28)	28(18)	15(17)	52(50)	0.1(0.1)
	$\eta_{min} > 1$	0.2(0.3)	21(26)	3.4(3.1)	0.4(0.4)	0.1(0.1)
nominal vertex ToF trigger	all events	66(73)	42(46)	68(72)	29(26)	65(70)
nominal vertex Ray trigger	all events	57(65)	8(14)	62(52)	0(0)	95(94)

8 Cross Section Measurement

To measure the total γp cross section we use data with the nominal vertex position, where the uncertainty in the luminosity calculation is significantly smaller than in the data taken with the shifted vertex position. However, as can be seen from Table 1 the efficiencies for the diffractive channels are higher in the shifted vertex data sample. Therefore, for the determination of the diffractive contributions to the γp cross section we use the data taken with shifted z-vertex position. The analysis and the cross checks are described in the following subsections 8.1 – 8.3.

8.1 Diffractive Contributions

To measure the diffractive γp cross sections we choose the variables in which a separation of diffractive and non-diffractive contributions is least model dependent. These variables, η_{max} and η_{min}, are related to the central rapidity gap in the hadronic final state.

For each event η_{max} is defined as the maximum pseudo-rapidity of all reconstructed charged tracks and all clusters in the LAr calorimeter with energy larger than 400 MeV. In diffractive events η_{max} indicates the maximum pseudo-rapidity of secondary hadrons from photon dissociation. It was shown in a recent H1 analysis of diffractive photoproduction [26] that the spectrum of η_{max} for non-diffractive events falls nearly exponentially with decreasing η_{max}, whilst the rate of photon diffractive dissociation depends only weakly on this variable. Events with elastic vector meson production have the largest possible width of the rapidity gap and are concentrated at lower values of the η_{max} spectrum.

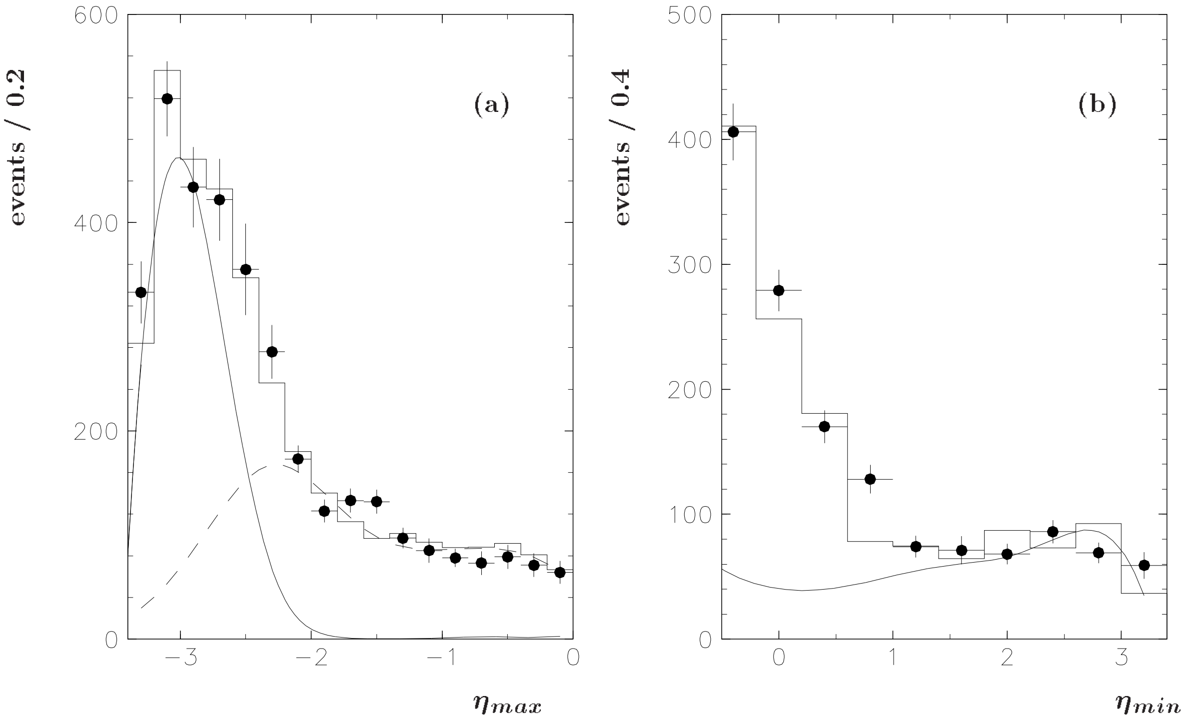

Figure 4: The η_{max} (a) and η_{min} (b) distributions for the sample with shifted vertex. The data are shown with solid circles. The histogram represents the result of a combined fit based on the PHOJET model summing all five contributions (EL, PD, GD, DD and ND) and using $\sigma_{DD} = 20$ μb. The full curve in (a) represents the sum of elastic and single proton dissociation. The sum of single photon and double dissociation contributions in (a) is represented by the dashed curve. The sum of single proton and double dissociation in (b) is shown by the full curve.

The η_{max} distribution for the data sample with shifted interaction vertex is shown in Fig. 4a, where we additionally require the calorimetric energy with $\eta > 1$ to be less than 1 GeV. This requirement reduces the contribution from non-diffractive events. MC calculations show that all four diffractive reactions contribute to the η_{max} spectrum in the range $-3.5 < \eta_{max} < 0$, whilst the contribution from non-diffractive processes is negligible. Below $\eta_{max} = -2$ the spectrum is dominated by elastic and single proton dissociation channels, where η_{max} is determined by the maximum pseudo-rapidity of the vector meson decay products. These two contributions are practically indistinguishable by shape, but have different efficiencies. For proton diffractive dissociation only the events with a low mass proton system ($M < 10$ GeV/c^2), where secondary particles escape detection very close to the proton beam direction, contribute to the η_{max} spectrum. The region $-2 < \eta_{max} < 0$ is dominated by single photon and double diffractive dissociation contributions, which have again a similar shape, but different acceptances.

The η_{min} variable is defined as the minimum pseudo-rapidity in the interval $-2 < \eta < 3.5$, of all charged tracks and of all calorimeter clusters with an energy larger than 400 MeV. An additional condition is that the event has a reconstructed charged track with $\eta < -2.4$. The latter condition is necessary for tagging a low mass hadronic system on the photon side. In diffractive events η_{min} indicates the minimum pseudo-rapidity of secondary hadrons from proton dissociation. The measured η_{min} distribution for the data sample with shifted interaction vertex is shown in Fig. 4b and is dominated by the non-diffractive contribution, which falls nearly exponentially with increasing η_{min}. However, there is a flat part of the spectrum with $\eta_{min} > 1$ caused by proton diffraction dissociation processes, where the mass of the hadronic system produced on the proton side is larger than about 5 GeV/c^2. Both single and double dissociation contributions have a similar shape. The acceptances for various partial processes to contribute to the η_{max} and η_{min} distributions are presented in Table 1, calculated using the PHOJET and PYTHIA MC models.

To obtain the diffractive γp cross sections we make a combined fit of the η_{max} and η_{min} distributions in the intervals $-3.5 < \eta_{max} < 0$ and $1 < \eta_{min} < 3.5$ using formula (4). In this fit procedure the shapes of the spectra for each partial contribution are fixed from the MC calculations, while the cross sections σ_i for single dissociation and elastic reactions are left as free fit parameters. Since only three of the four diffractive cross sections can be reliably extracted from the fit we make an additional assumption about the value of the double dissociation cross section varying it from 0 to 40 μb. The upper limit is chosen to be about two times larger than the value expected from the low energy measurements extrapolated using Regge-type formalism [27]. Our attempts to determine the double dissociation contribution directly from the data by observing a high mass dissociation of both the proton and the photon give results within this interval, but are inconclusive. In order to estimate the contribution of the tail of the non-diffractive reaction into the fitted η_{min} region, the non-diffractive cross section was fixed in the fit to describe the part of the η_{min} spectrum below $\eta_{min} = 1$. An example of a fit using the PHOJET model and the assumption $\sigma_{DD} = 20$ μb is shown in Fig.4. The fit describes the data well. The cross sections σ_{EL}, σ_{GD} and σ_{PD} obtained are displayed in Fig.5a as functions of σ_{DD}. The errors are dominated by systematic uncertainties due to model dependence and are shown by grey bands.

The model dependence was studied by using different MC generators (PYTHIA and PHOJET) and, in addition, by varying the main parameters of the diffractive model within the MC generator. These parameters are the value of the nuclear slope B, the minimum value for the mass of the dissociated system and the form of the mass dependence of the cross section:

- The value of the *nuclear slope* was varied by $\Delta B = \pm 4$ (GeV/c)$^{-2}$ in the elastic process and half this range in the single dissociation processes. This represents a conservative estimate of the uncertainty in the extrapolations of the measured slope from lower energies [18].

- The uncertainty in the description of the measured *low mass part* of the dissociated mass spectrum [18, 19] was conservatively estimated by increasing the value of the minimum mass of the diffractively produced hadronic system by 0.2 GeV/c^2.

- *Mass dependence* of single and double diffractive dissociation. The photoproduction data at lower energy [18] and hadron hadron diffractive dissociation at $\sqrt{s} = 546$ GeV [28] are well described by a phenomenological $1/M^2$ dependence. This mass dependence is implemented in the MC models used for the analysis. However, the predictions of Regge theory with a supercritical pomeron trajectory give after an integration over t $1/M^{2\alpha(0)}$, where $\alpha(0)$ is the value of the intercept of the pomeron trajectory at $t = 0$. The phenomenological fit of the total cross section [4] gives $\alpha(0) = 1.08$. In order to estimate this part of the model dependence we set the mass distribution also to $1/M^{2.2}$ in the MC calculations.

For every variation of a parameter we average the results and ascribe half of the spread to be the corresponding systematic error. This is then added to other errors in quadrature. Similarly, we average the results obtained with the PYTHIA and PHOJET models. The final results are

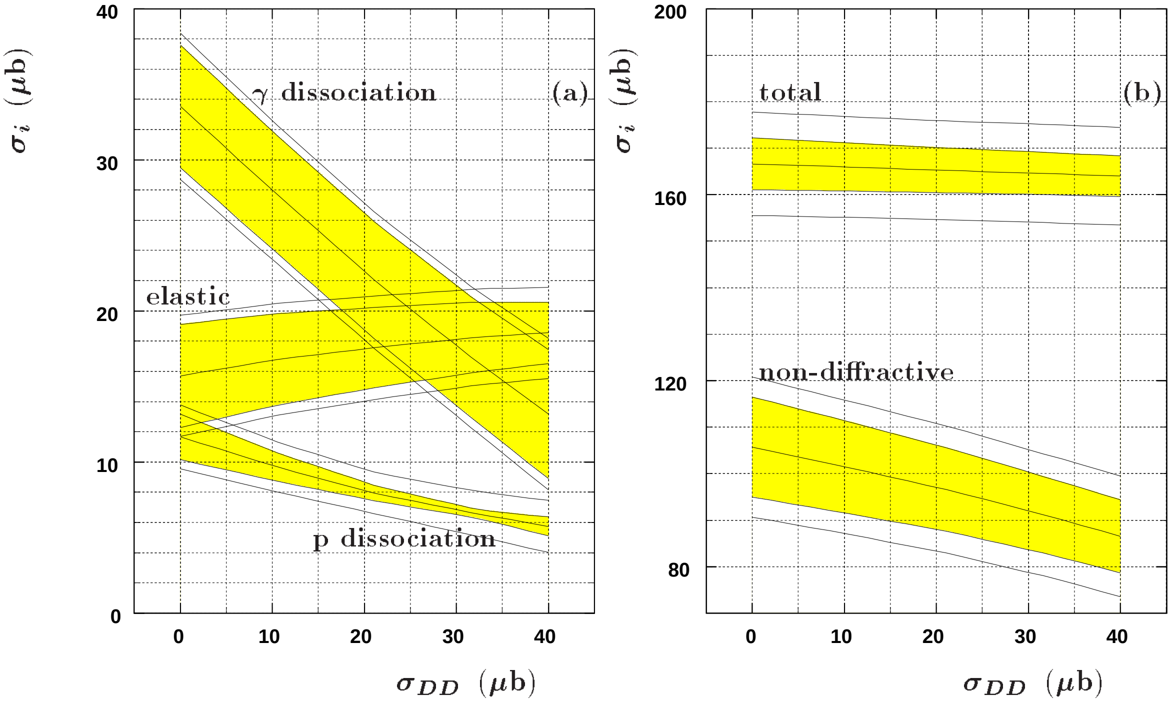

Figure 5: The measured partial diffractive (a) and non-diffractive and total (b) γp cross sections as a function of the assumed double dissociation cross section. The errors are shown as bands of ± 1 standard deviation. The wide bands correspond to full statistical and systematic errors added in quadrature. The narrow grey bands show the systematic errors due to the model dependence described in the text.

shown in Fig.5a. The wider bands correspond to full statistical and systematic errors added in quadrature. The narrower grey bands show the contribution to the systematic errors from the model dependence described above. The main sources of the model independent contribution to the systematic errors are the uncertainties in the luminosity measurement (5.6%), in the acceptance of the electron tagger (5.0%, which affect all the results) and an uncertainty in the statistical background subtraction affecting only the elastic channel (8%). The statistical errors are much smaller than the systematic errors in all cases except for proton dissociation where they are comparable. Variation of the non-diffractive contribution to the fitted distributions by a factor of two, changing the fit interval and variation of the different requirements used for the data selection alter the results only within the statistical errors.

One can see from Fig.5a that the elastic cross section is almost independent of any assumption made about σ_{DD}. Proton dissociation and especially photon dissociation show a stronger correlation with the assumed value of σ_{DD}. However, at any value of σ_{DD}, the single photon dissociation is substantially larger than the single proton dissociation, in contrast to the assumption that they are equal, made in earlier $\sigma_{tot}^{\gamma p}$ analyses [2, 3] at HERA.

The values of the diffractive cross sections averaged over σ_{DD}, are presented in Table 2.

8.2 Non-Diffractive and Total Cross Sections

The measurement of the total γp and non-diffractive cross sections is based on the ToF-triggered sample with the nominal vertex. The efficiencies for the different subprocesses are given in Table 1. As mentioned above, the efficiencies for elastic and proton diffraction channels using nominal vertex are about half those for shifted vertex data making the determination of diffractive contributions from the nominal vertex sample less reliable. The diffractive cross sections are

Table 2: Results for partial and total γp cross sections under the assumption that the double dissociation cross section is in the range $0 < \sigma_{DD} < 40$ μb. The first error is statistical, the second one is systematic, and the third error reflects the systematic uncertainty due to the assumption on σ_{DD} . Their sum in quadrature is given as the full error. Note, that due to the error correlation in the partial cross sections the error of the total cross section is relatively smaller.

process	*cross section* (μb)	*full error* (μb)
$\sigma(\gamma p \to XY)$, *DD*	20 ± 20 (assumed)	—
$\sigma(\gamma p \to Xp)$, *GD*	$23.4 \pm 2.6 \pm 4.3 \pm 10.2$	11.3
$\sigma(\gamma p \to VY)$, *PD*	$8.7 \pm 1.5 \pm 1.5 \pm 3.0$	3.6
$\sigma(\gamma p \to Vp)$, *EL*	$17.1 \pm 1.6 \pm 3.7 \pm 1.4$	4.3
EL + GD + PD + DD	$69.2 \pm 3.4 \pm 8.8 \pm 9.3$	13.2
ND	$96.1 \pm 3.5 \pm 14.7 \pm 9.6$	17.9
Total	$165.3 \pm 2.3 \pm 10.9 \pm 1.3$	11.2

therefore assumed to be those found from the shifted vertex data, as described in the previous section, and the nominal vertex data are used to determine only the missing non-diffractive cross section. This was done by solving eq.(4) for σ_{ND}, then calculating $\sigma_{tot}^{\gamma p}$ as a sum over five partial contributions, all errors being properly propagated including a correlation between diffractive and non-diffractive cross sections.

The σ_{ND} and $\sigma_{tot}^{\gamma p}$ obtained as a function of the assumed value of σ_{DD} are shown in Fig.5b. The model dependence displayed has been studied in exactly the same way as in the analysis above. The model uncertainty of $\sigma_{tot}^{\gamma p}$ and σ_{ND} is dominated by the difference between PHOJET and PYTHIA models which enters the calculations via the different efficiencies for the ND, GD and DD channels shown in Table 1.

The total cross section is remarkably insensitive to assumption about σ_{DD} and changes only by 2.6 μb as σ_{DD} varies between 0 and 40 μb. This is because the efficiencies ε_i for GD, DD and ND are very similar (see Table 1). The sum $\sigma_{GD} + \sigma_{DD} + \sigma_{ND}$ is therefore practically fixed by eq.(4), whilst the total contribution of σ_{PD} and σ_{EL} in eq.(4) is weakly dependent on σ_{DD}.

The results, averaged over σ_{DD} =0–40 μb are given in Table 2 along with the diffractive cross sections. We finally obtain the total photoproduction cross section for an average $W_{\gamma p}$ of 200 GeV

$$\sigma_{tot}^{\gamma p} = 165.3 \pm 2.3(\text{stat.}) \pm 10.9(\text{syst.})\ \mu\text{b}.$$

The statistical error reflects all the relevant statistical uncertainties for the shifted and nominal vertex data samples, as well as those from the MC calculations. The various contributions to the systematic errors are listed in Table 3. The dominant sources are the uncertainty of the e-tagger acceptance ($\pm 8.5\mu$b) and the difference between the PYTHIA and PHOJET models ($\pm 5.1\mu$b).

8.3 Cross Checks of the Total Cross Section Measurement

The data taken with the Ray-trigger allow a cross check of the model-dependent acceptances ε_i. Since ToF is sensitive only to particles with $\eta < -2$ and the Ray trigger is fired by particles around $\eta = 0$, the two triggers are quite independent of each other. We have compared the

Table 3: Different contributions to the systematic error of the $\sigma_{tot}^{\gamma p}$ measurement.

Source	*Error* (μb)	
	ToF-trigger	*Ray-trigger*
assumption of $\sigma_{DD} < 40\mu$b	1.3	5.4
efficiency uncertainty due to model dependence	5.6	5.7
syst. errors of diffr. cross sections (without model dependence)	1.3	4.2
1.6% uncertainty in the luminosity measurement	2.8	
0.4% uncertainty in the fraction of luminosity in satellite bunches	0.5	
5% uncertainty in the e-tagger acceptance	8.5	
1% uncertainty in QED radiative corrections	1.7	
Total	10.9	12.7

fraction of ToF-triggered events in the Ray-triggered data sample with predictions from the MC simulations. This fraction is 70% in the data, which is 2% higher than the fraction calculated with the PHOJET model and 3% lower than that predicted by the PYTHIA model. This cross check suggests that the true value of the acceptance lies between the PYTHIA and PHOJET estimates, and validates our procedure of averaging the cross sections over the two models.

A second determination of the cross section has been made using the Ray-trigger data sample, giving $\sigma_{tot}^{\gamma p} = 162 \pm 2 \pm 13$ μb. Here the relative contributions of the subprocesses are taken from the above measurements (section 8.1) for different values of σ_{DD}. This second determination of $\sigma_{tot}^{\gamma p}$ is consistent with the first result described above. The larger systematic error of this result reflects the larger difference in the efficiency for different reactions in the Ray-trigger data sample, compared to those in the sample taken with the ToF-trigger. The Ray-trigger selection has a higher acceptance for the non-diffractive reactions, but shows a nearly vanishing efficiency for the elastic and the single proton dissociation processes. In addition, since it depends strongly on the transverse momentum and multiplicity of charged particles, the Ray-trigger has a higher sensitivity to the details of the hadronic final state simulation. The contributions to the systematic error of this measurement are also given in Table 3.

A determination using only the shifted vertex data resulted in $\sigma_{tot}^{\gamma p} = 166 \pm 2 \pm 15$ μb. The larger systematic error is a result of the larger uncertainty of the luminosity measurement.

9 Discussion

The energy dependence of $\sigma_{tot}^{\gamma p}$ is shown in Fig. 6 with the low energy data [29] and the present measurement together with a recent result from ZEUS [3]. The data are compared with predictions made by A.Donnachie and P.V.Landshoff (DL) [4] and H.Abramovich, E.M.Levin, A.Levy and U.Maor (ALLM) [5]. The DL curve presents a parameterization of a universal rise of the cross section in hadron hadron and low energy photon hadron collisions. In this parameterization the high energy cross section behaviour is described by a function $W_{\gamma p}^{2\Delta}$ with $\Delta = 0.0808$. The dotted line in Fig. 6 represents a further DL-type parameterization, which takes into account the recent CDF measurement of the total $p\bar{p}$ cross section [8] with $\Delta = 0.11$. The ALLM is a Regge-type cross section parameterization for real and virtual photon proton collisions with $\Delta = 0.045$.

In Fig. 5 the measurement of the diffractive cross section contributions is shown as a function of the assumed value for the double diffractive dissociation γp cross section. One should note

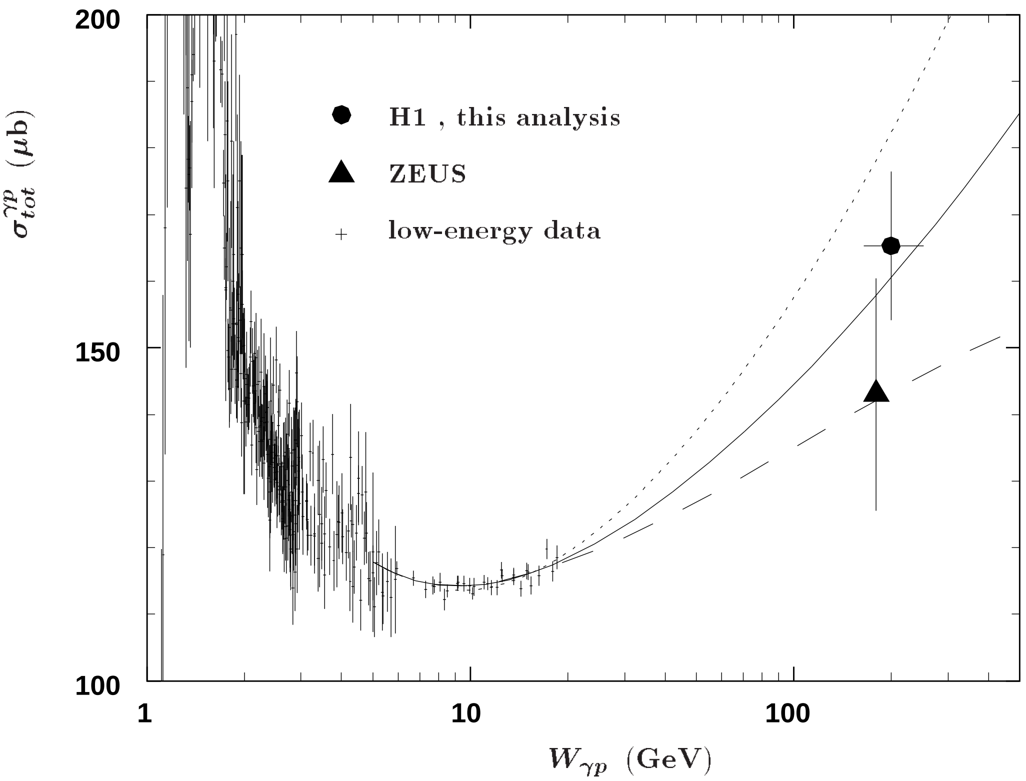

Figure 6: Total photoproduction cross section as a function of the γp centre of mass energy $W_{\gamma p}$. The solid line is the prediction of the DL [4] combined fit of hadron hadron and low energy photoproduction data and the dashed line is the ALLM [5] parameterization. The dotted line presents the DL parameterization obtained after the recent measurement of the total $p\bar{p}$ cross section by CDF [8].

that the results presented here on photon and proton diffractive dissociation cross sections are the first measurements of these quantities at HERA energies. This measurement can be compared with predictions of A.Capella, A.Kaidalov, C.Merino and J.Tran Thanh Van (CKMT) [30], G.A.Schuler and T.Sjöstrand (SaS) [31], and E.Gotsman, E.M.Levin and U.Maor (GLM) [7][3]. These models are based on different assumptions about the structure and dissociation of the photon and the proton. From these models only the CKMT predictions are based on theoretical calculations using the Regge model, taking into account absorptive corrections for all the diffractive reactions measured here. The comparison of these models with the data is shown in Table 4, where the data are presented for a fixed value of the double dissociation cross section ($\sigma_{DD} = 15\mu$b). This particular choice is made according to the predictions of the models. The predictions for the elastic reaction are in good agreement with the H1 measurement as well as with the recent result from the ZEUS collaboration ($18 \pm 7\,\mu$b) [3]. However, the relative contribution of single proton dissociation is observed to be about three times lower than that of photon dissociation. This observation disagrees with the predictions of the SaS and GLM models. In the latter the ratio of the proton to the photon single diffractive dissociation is obtained using the quark counting rule. The results of the CKMT calculations are supported by the present measurement.

[3]The published results of the GLM calculation are scaled to a dissociation mass interval of $M^2 < 0.1 W_{\gamma p}^2$.

Table 4: The comparison of the diffractive cross section calculations with the H1 measurement. The data are presented for a fixed value $\sigma_{DD} = 15\mu$b.

Reaction	*Cross Sections* (μb)			
	Data	CKMT	SaS	GLM
$\sigma(\gamma p \to Vp),\ EL$	17 ± 4	17	16	17
$\sigma(\gamma p \to Xp),\ GD$	26 ± 5	25	13	18
$\sigma(\gamma p \to VY),\ PD$	9 ± 2	7	10	15
$\sigma(\gamma p \to XY),\ DD$	15	15	13	15

10 Conclusion

Using the H1 detector at HERA results on γp scattering at the average c.m. energy of $W_{\gamma p} = 200$ GeV are obtained. The total photoproduction cross section is measured to be $\sigma_{tot}^{\gamma p} = 165 \pm 2\ (stat.) \pm 11\ (syst.)\ \mu$b replacing our previous result [2]. The extracted diffractive and non-diffractive contributions to the cross section are presented as a function of the assumed value for the double diffractive dissociation cross section σ_{DD} . The cross section of single photon diffractive dissociation is observed to be substantially higher than the single proton diffractive dissociation cross section. The elastic cross section depends only weakly on the assumption made on σ_{DD} and is found to be $17.1 \pm 4.3\ \mu$b .

Acknowledgments

We are grateful to the HERA machine group whose outstanding efforts made this experiment possible. We appreciate the immense effort of the engineers and technicians who constructed and maintain the detector. We thank the funding agencies for their financial support of the experiment. We wish to thank the DESY directorate for the hospitality extended to the non-DESY members of the collaboration. We are indebted to R.Engel and T.Sjöstrand for help concerning the MC event generators used in this analysis. The stimulating discussions with M.Ryskin and A.Kaidalov are gratefully acknowledged.

References

[1] Particle Data Group, L.Montanet et al., Phys. Rev. D50 (1994) 1173

[2] H1 Collab., T.Ahmed et al., Phys. Lett. B299 (1993) 374
S.Levonian, Proc. of the XXVIIIth Rencontre de Moriond, ed. J.Tran Thanh Van, (Edition Frontieres, 1993) 529

[3] ZEUS Collab., M.Derrick et al., Z.Phys. C63 (1994) 391

[4] A.Donnachie and P.V.Landshoff, Phys. Lett. B296 (1992) 227

[5] H.Abramovich, E.M.Levin, A.Levy and U.Maor, Phys. Lett. B269 (1991) 465

[6] A.Capella, A.Kaidalov, C.Merino and J.Tran Thanh Van, Phys.Lett. B337 (1994) 358

[7] E.Gotsman, E.M.Levin and U.Maor, Phys. Lett. B347 (1995) 424

[8] CDF Collab., F.Abe et al., Phys.Rev.D50 (1994) 5550

[9] C.F.Weizsäcker, Z.Phys.88 (1934) 612;
E.J.Williams, Phys.Rev. 45 (1934) 729;
S.Frixione et al., Phys. Lett. B319 (1993) 339

[10] A.I.Lebedev, Proc. Workshop on Physics at HERA, eds. W.Buchmüller and G.Ingelman, DESY (1991) 613

[11] T.H.Bauer et al., Rev.Mod.Phys. 50 (1978) 261

[12] T.Sjöstrand, CERN-TH-6488 (1992), Comput. Phys. Commun. 82 (1994) 74

[13] R.Engel, Proceedings of the XXIXth Rencontre de Moriond, ed. J.Tran Thanh Van, (Edition Frontieres, 1994) 231

[14] T.Sjöstrand and M.van Zijl, Phys. Rev. D36 (1987) 2019

[15] A.Capella et al., Phys.Rep. 236 (1994) 227

[16] P.Aurenche et al., Comp.Phys.Commun. 83 (1994) 107

[17] R.Engel, Z.Phys. C66 (1995) 203

[18] T.J.Chapin et al., Phys.Rev. D31 (1985) 17

[19] K.Goulianos, Phys.Rep., 101 (1983) 170

[20] A.Kwiatkowski, H.Spiesberger and H.J.Möhring, Workshop on Physics at HERA, eds. W.Buchmüller and G.Ingelman, DESY (1991) 1294

[21] H1 Collab., I.Abt et al., "The H1 detector at HERA", DESY preprint 93-103 (1993)

[22] H1 Calorimeter Group, B.Andrieu et al., Nucl. Instr. and Meth. A336 (1993) 460

[23] H.Bethe and W.Heitler, Proc. Roy. Soc. A146 (1934) 83

[24] H1 Collab., T.Ahmed et al., Z.Phys. C66 (1995) 525

[25] S.P.Baranov et al., Workshop on Physics at HERA, DESY (1991) 1478

[26] H1 Collab., T.Ahmed et al., Nucl.Phys. B435 (1995) 3

[27] K.Goulianos, Nucl.Phys.B (Proc.Suppl) 12 (1990) 110

[28] UA4 Collab., D.Bernard et al., Phys. Lett. B186 (1987) 227

[29] A.Baldini et al., Landolt-Börnstein's New Series I/12B (1988) 345

[30] A.Capella et al., Phys. Lett. B343 (1995) 403
A.Kaidalov, private communication (only a sum of the diffractive cross sections is given in ref. [30].)

[31] G.A.Schuler and T.Sjöstrand, Nucl.Phys. B407 (1993) 539